

MIRReS: Multi-bounce Inverse Rendering using Reservoir Sampling

Yuxin Dai, Qi Wang, Jingsen Zhu, Dianbing Xi, Yuchi Huo, Chen Qian, Ying He

Abstract—We present MIRReS, a novel two-stage inverse rendering framework that jointly reconstructs and optimizes the explicit geometry, material, and lighting from multi-view images. Unlike previous methods that rely on implicit irradiance fields or simplified path tracing algorithms, our method extracts an explicit geometry (triangular mesh) in stage one, and introduces a more realistic physically-based inverse rendering model that utilizes multi-bounce path tracing and Monte Carlo integration. By leveraging multi-bounce path tracing, our method effectively estimates indirect illumination, including self-shadowing and internal reflections, which improves the intrinsic decomposition of shape, material, and lighting. Moreover, we incorporate reservoir sampling into our framework to address the noise in Monte Carlo integration, enhancing convergence and facilitating gradient-based optimization with low sample counts. Through qualitative and quantitative evaluation of several scenarios, especially in challenging scenarios with complex shadows, we demonstrate that our method achieves state-of-the-art performance on decomposition results. Additionally, our optimized explicit geometry enables applications such as scene editing, relighting, and material editing with modern graphics engines or CAD software. **The source code is available at <https://brabbitdousha.github.io/MIRReS/>**

Key Words and Phrases—Inverse rendering, path tracing, multi-view 3D reconstruction, relighting, computer graphics.

1. Introduction

Inverse rendering, the process of decomposing multi-view images into geometry, material and illumination, is a long-standing challenge in computer graphics and computer vision. The task is particularly difficult and ill-posed due to the ambiguity inherent in finding solutions that can produce the same observed image, especially in the absence of constraints on illumination conditions.

Recent advancements in neural radiance fields (NeRFs) [1] and neural implicit surfaces (SDFs) [8], [9] have spurred several works [15], [17]–[21] that employ NeRF or SDF as the scene representation. These methods often utilize auxiliary neural networks to predict materials or illumination.

- *Corresponding author: Y. He (email: yhe@ntu.edu.sg)*
- *Y. Dai and Y. He are with the College of Computing and Data Science, Nanyang Technological University, Singapore.*
- *Q. Wang, J. Zhu, D. Xi, and Y. Huo are with the State Key Laboratory of CAD&CG, Zhejiang University, China.*
- *C. Qian is with SenseTime Research, China.*

However, these MLP-based methods are limited by insufficient network capacity and inefficient convergence, leading to distorted reconstructed geometry and inaccurate material. On the contrary, TensoIR [22] leverages a more compact and efficient TensoRF-based [5] scene representation, enabling explicit second-bounce ray marching online and producing a more accurate indirect illumination estimation. Although these implicit methods have achieved remarkable results, they still have two **inherent disadvantages**: Firstly, they represent geometry as implicit density fields rather than triangular meshes, which limits their applicability in the CG industry, where triangular meshes are the most widely accepted digital assets. Secondly, while some methods explicitly sample secondary rays for indirect illumination, they rely on radiance fields instead of physically-based rendering (PBR) to obtain the second-bounce radiance. This approach lacks physically-based constraints on the optimized materials, resulting in inaccurate material optimization.

To address the above two problems, we propose a **mesh-based** two-stage inverse rendering framework called *MIRReS*¹ that jointly decomposes geometry, PBR material, and illumination from multi-view images while modeling indirect illumination by physically-based *multi-bounce* path tracing. Our inverse rendering framework directly optimizes triangle meshes to enable applications such as scene editing, relighting, and material editing compatible with modern graphics engines or CAD software (see Figure 1). Additionally, the explicit triangular mesh representation allows us to implement efficient path tracing using modern graphics hardware, making it possible to compute multi-bounce path tracing within acceptable timeframes. However, existing mesh-based neural inverse rendering methods, *e.g.* NVdiffrec-MC [14], suffer from unstable geometry optimizations, leading to artifacts such as holes and self-intersecting faces. The unstable geometry limits the accuracy of ray-mesh intersection and makes path tracing intractable, especially in multi-bounce cases where errors will accumulate recursively.

In particular, our paper introduces three key technologies: (a) **Mesh optimization**. Inspired by NeRF2Mesh [11], we employ a two-stage geometry optimization and refinement process. In stage 1, we train an off-the-self NeRF-based model (InstantNGP [4] and NeuS2 [24]) and extract a coarse mesh as the geometry initialization. In stage 2, we refine the mesh by adjusting the vertices’ position to minimize rendering errors. (b) **Indirect illumination estimation**.

1. Name taken from “Multi-bounce Inverse Rendering using Reservoir Sampling”.

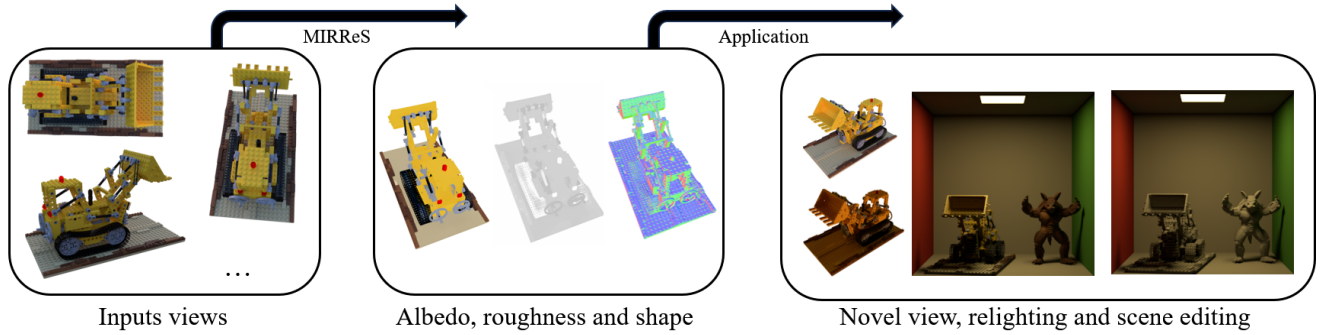


Figure 1. Given multi-view images of a scene, our method achieves high-quality geometry and materials optimization, enabling multiple applications such as novel view synthesizing, relighting, and scene editing.

We explicitly conduct physically-based multi-bounce path tracing with Monte Carlo integration to estimate the indirect illumination in stage 2. This strategy imposes stronger physical constraints on the material, resulting in more accurate indirect illumination and relighting. (c) **Convergence acceleration.** The Monte Carlo estimator requires a large sample count to ensure the accuracy of optimization, which significantly slows down the convergence speed. Therefore, we novelly incorporate reservoir sampling of the direct illumination [25] into our inverse rendering framework to reduce the sample count while maintaining relatively small noise. Meanwhile, coupled with a denoiser inspired by NVdiffrec-MC [14], our framework can achieve optimization with a small sample count, leading to a considerable acceleration in convergence.

By evaluating several scenarios, especially in challenging scenarios with complex shadows, we show that our method achieves state-of-the-art performance on the decomposition and relighting results. To summarize, the major contributions of this paper include:

- 1) We propose MIRReS, a physically-based inverse rendering framework that jointly optimizes the geometry, material and lighting from multi-view input images, achieving state-of-the-art results in mesh recovery, material-lighting decomposition and relighting.
- 2) Our method utilizes *multi-bounce path tracing* to estimate indirect illumination more accurately and successfully achieves promising decomposition results in the challenging highly-shadowed scenes.
- 3) Our method utilizes *Reservoir-based Spatio-Temporal Importance Resampling* for direct illumination, which can greatly reduce the sample counts and accelerate the rendering process.

2. Related work

Neural scene representations As an alternative to traditional representations (*e.g.* mesh, point clouds, volumes, *etc.*), neural representations have achieved great success

in novel view synthesis and 3D modeling. Neural radiance fields (NeRF) [1] uses MLPs to implicitly encode a scene as a neural field of volumetric density and RGB radiance values, and uses volume rendering to produce promising novel view synthesis results. To address the limited expression ability and slow speed of the vanilla MLP representation, follow-up works leverage voxels [2], [3], hashgrids [4], tensors [5], polygon rasterization [6], adaptive shells [7], *etc.* to achieve high-fidelity rendering result and real-time rendering speed. In addition to NeRF-based methods, 3D Gaussian Splatting (3DGS) [10] proposes to use point-based 3D Gaussians to represent a scene, enabling fast rendering speed due to the utilization of rasterization pipeline, stimulating follow-up works on quality improvement or many other applications [16], [43], [44]. Some other works also seek to combine neural and traditional representations, leveraging the strengths of both. For example, NeRF2Mesh [11] designs a two-stage reconstruction pipeline, which refines the textured mesh surface extracted from the NeRF density field to obtain delicate textured mesh recovery. In this work, we also employ a two-stage geometry optimization strategy combining neural implicit representation and triangle meshes.

Inverse rendering The task of inverse rendering aims to estimate the underlying geometry, material and lighting from single or multi-view input images. Due to inherent ambiguity between the decomposed properties and the input images, inverse rendering is an extremely ill-posed problem. Some methods simply the problem under constrained assumptions, such as controllable lights [26]–[28]. Physically-based methods [31], [32], [34], [35] account for global illumination effects via differentiable light transports and Monte-Carlo path tracing. The emergence of neural representations has stimulated abundant neural inverse rendering frameworks [15], [22], [30], which utilize neural fields as the positional functions of material and geometry properties, along with lighting as trainable parameters such as Spherical Harmonics (SH), Spherical Gaussian (SG), environment maps, *etc.*, and then jointly optimize them by rendering loss via differentiable rendering. However, neural fields also face challenges, such as low expressive capacity and high com-

Table 1. COMPARISON BETWEEN EXISTING INVERSE RENDERING METHODS AND OUR METHOD.

| Method | Geometry | Lighting | Indirect Lighting | Sampling |
|--------------|----------|-------------------|-------------------|---------------------|
| NeRFactor | Implicit | Environment | ✗ | N/A |
| TensoIR | Implicit | Ray tracing | ✓ | Importance Sampling |
| NVdiffrec-MC | Mesh | Path tracing (PT) | ✗ | Importance Sampling |
| NeILF++ | Implicit | Implicit | ✓ | Stratified Sampling |
| GS-IR | 3DGS | Split-sum | ✓ | N/A |
| Ours | Mesh | Multi-bounce PT | ✓ | Reservoir Sampling |

putational overhead caused by ray marching. Meanwhile, other methods also utilize explicit geometry representations, such as mesh [14], [29] or 3D Gaussian [10], [16]. Table 1 lists representative recent inverse rendering methods and compares their settings with our method. Implicit geometry representation requires frequent MLP queries to compute ray intersection, leading to worse performance than explicit representations such as mesh. In this work, we choose mesh as the scene geometry and utilize multi-bounce raytracing that enables superior capability to capture complex indirect lighting. Our method is the first inverse rendering framework that supports multi-bounce raytracing to estimate indirect lighting more accurately.

3. Method Overview

In this section, we’ll describe our proposed inverse rendering framework using multi-bounce raytracing and reservoir sampling. Given multi-view image captures of an object illuminated by unknown environment lighting conditions, together with their corresponding camera poses, our method jointly reconstructs the geometry, spatially-varying materials and environment lighting. Unlike most recent works using neural implicit geometry representations (*e.g.* NeRF or neural SDF), which have significant limitations as introduced in Section 1, our method opts for triangle mesh as an explicit geometry representation. However, It would be difficult to optimize the mesh topology directly from multi-view input images without a reasonable initialization. Inspired by NeRF2Mesh [11], we employ a two-stage training process: the first stage trains a neural radiance and SDF field to extract a coarse mesh from input images, while the second stage, *which is the major part of our pipeline*, simultaneously optimizes scene material and lighting through our physically-based rendering and refines the mesh geometry. Figure 2 shows an overview of our pipeline.

3.1. Stage 1: Radiance Field and Coarse Mesh Acquisition

The main purpose of this stage is to initialize a radiance field and geometry to facilitate optimization in stage 2. We use an efficient off-the-shelf NeRF-based method (Instant-NGP [4]) to train a neural radiance field and a neural density

field:

$$\sigma, \mathbf{f} = F_\sigma(\mathbf{x}) \quad (1)$$

$$\mathbf{c} = F_c(\mathbf{x}, \mathbf{d}, \mathbf{f}) \quad (2)$$

where F_σ and F_c refer to the density field and the radiance field respectively, \mathbf{f} represents an intermediate feature vector, σ and \mathbf{c} denote the density and radiance at position \mathbf{x} , and \mathbf{d} refers to the view direction. We regard the converged F_c as our initial radiance field.

We can already extract the coarse mesh from the density field F_σ using marching cube. However, due to the inherent lack of geometric constraints in the NeRF-based volumetric representation, the extracted geometry usually contains artifacts like holes or sawteeth, negatively affecting the optimization in stage 2. Therefore, we additionally use a SOTA SDF reconstruction method (NeuS2 [24]) to extract the coarse mesh $\mathcal{M}_{\text{coarse}} = \{\mathcal{V}, \mathcal{F}\}$ (where \mathcal{V} denotes vertices and \mathcal{F} denotes faces). The density field F_σ will then be discarded in the next stage, while F_c will continue to be optimized in stage 2 for geometry refinement.

3.2. Stage 2: mesh refinement and intrinsic decomposition

Given the coarse mesh $\mathcal{M}_{\text{coarse}}$ and radiance field F_c obtained from stage 1, the goal of this stage is to decompose material and environment lighting parameters, as well as refine the geometry of $\mathcal{M}_{\text{coarse}}$ into a fine mesh $\mathcal{M}_{\text{fine}}$.

Rendering Given the extracted mesh \mathcal{M} and a camera ray $\mathbf{r}(t) = \mathbf{o} + t\mathbf{d}$ from origin \mathbf{o} in direction \mathbf{d} , we firstly use `nvdiffrastr` [12] to compute the ray-mesh intersection:

$$\mathbf{x} = \text{intersect}(\mathbf{r}, \mathcal{M}) \quad (3)$$

This process is differentiable, making it possible to conduct differentiable rendering and gradient descent optimization afterward. Our pipeline jointly employs 2 rendering methods (which will be used by the tasks of mesh refinement and intrinsic decomposition, respectively), including radiance field rendering and physically-based surface rendering.

Radiance field rendering We make use of the appearance field F_c in the NeRF network in the first stage to produce the rendering result. Unlike NeRF which uses ray marching and volume rendering, we directly feed the intersected surface point \mathbf{x} from Eq. (3) into the appearance field to produce the rendered ray color $C_{\text{RF}}(\mathbf{r})$:

$$C_{\text{RF}}(\mathbf{r}) = F_c(\mathbf{x}, \mathbf{d}, \mathbf{f}). \quad (4)$$

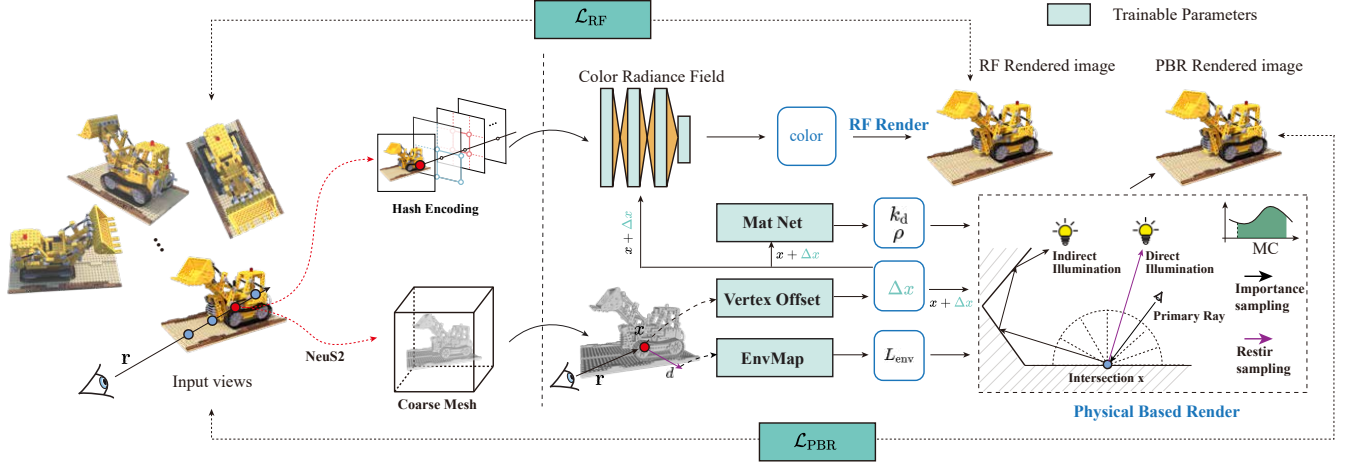


Figure 2. An overview of our pipeline.

Physically-based surface rendering Given the surface shading point \mathbf{x} , we render the shading color through the rendering equation [33], which is an integral over the upper hemisphere Ω at \mathbf{x} :

$$C_{\text{PBR}}(\mathbf{r}) = \int_{\Omega} L_i(\mathbf{x}, \omega_i) f_r(\mathbf{x}, \omega_i, \mathbf{d}, \mathbf{m})(\omega_i \cdot \mathbf{n}) d\omega_i, \quad (5)$$

where $L_i(\mathbf{x}, \omega_i)$ denotes the incident lighting from direction ω_i , \mathbf{m} denotes the spatially-varying material parameters at \mathbf{x} , f_r denotes the bidirectional reflectance distribution function (BRDF), and \mathbf{n} denotes the surface normal at \mathbf{x} .

In the context of multi-bounce path tracing, the incident light $L_i(\mathbf{x}, \omega_i)$ is the composition of direct light, which is the environment illumination in this work, and the indirect light:

$$L_i(\mathbf{x}, \omega_i) = V(\mathbf{x}, \omega_i) L_{env}(\omega_i) + L_{ind}(\mathbf{x}, \omega_i), \quad (6)$$

where $V(\mathbf{x}, \omega_i)$ is the light visibility function. In the next section, we'll describe how we estimate the direct (Section 4.1) and indirect (Section 4.2) lighting and render the result in detail.

Mesh refinement As mentioned in Section 1, implicit geometry representation may introduce bias and inaccuracy in indirect illumination estimation. Therefore, we opt to optimize a triangular mesh to represent scene geometry. DMtet [41] used by NVdiffrec-MC [14] is an existing approach for direct mesh optimization, but it suffers from topological inconsistencies and geometric instability, which in turn affects the accuracy of path tracing. Instead, we opt for a stable and continuous optimization approach. Inspired by NeRF2Mesh [11], we assign a trainable offset $\Delta \mathbf{v}_i$ to each mesh vertex $\mathbf{v}_i \in \mathcal{V}$ to refine the geometry, and optimize them along with the appearance fields F_c by minimizing the loss of radiance rendering. Specifically, given a camera s with known intrinsic and extrinsic parameters and its reference image $I_{\text{ref}}(s)$, we use radiance field rendering (Eq. (4)) to produce an image $I_{\text{RF}}(s)$, and then optimize

$\Delta \mathbf{v}_i$ and the parameters of F_c by minimizing the L2 loss between the rendering result and reference image:

$$\mathcal{L}_{\text{RF}} = \|I_{\text{RF}}(s) - I_{\text{ref}}(s)\|_2^2 \quad (7)$$

Similarly, we also use physically-based surface rendering (Eq. (5)) to produce an image $I_{\text{PBR}}(s)$. Thanks to the differentiability of nvdiffrast's ray-mesh intersection calculation, the gradient of the L2 loss between the PBR rendering result and the reference image can be back-propagated to $\Delta \mathbf{v}_i$:

$$\mathcal{L}_{\text{PBR}} = \|I_{\text{PBR}}(s) - I_{\text{ref}}(s)\|_2^2 \quad (8)$$

In summary, $\Delta \mathbf{v}_i$ is jointly optimized by \mathcal{L}_{RF} and \mathcal{L}_{PBR} in stage 2, which refines the geometry from $\mathcal{M}_{\text{coarse}}$ to $\mathcal{M}_{\text{fine}}$. Since $\Delta \mathbf{v}_i$ is continually changing during the optimization and does not change the face topology of the mesh, our mesh refinement approach ensures geometry stability and enables the introduction of multi-bounce path tracing.

Intrinsic decomposition Based on the mesh geometry, we now describe how we represent and optimize the spatially-varying material and environment lighting.

We adopt the physically-based BRDF model from Disney [13], combining a Lambertian diffuse term with a specular GGX lobe. The BRDF model requires 2 material parameters: diffuse albedo and roughness. We encode the spatially-varying material parameters of the scene using a neural field F_m , which predicts the material parameters \mathbf{m} given an input position \mathbf{x} : $\mathbf{m} = F_m(\mathbf{x})$.

We implement F_m as a small MLP with a multi-resolution hashgrid, following InstantNGP [4]. The predicted \mathbf{m} is a 4-channel vector, which will be further split by channel into the diffuse albedo (3), roughness (1). Please refer to our supplementary material for a specific description of the BRDF model.

Following NVdiffrec-MC [14], we represent the environment lighting as a high dynamic range environment map with 128×256 pixels, where all pixel colors are trainable parameters.

4. Direct and indirect lighting

As described in Eq. (6), the incident lighting in the rendering equation is divided into 2 components (direct and indirect), which are estimated through reservoir sampling (Section 4.1) and multi-bounce raytracing (Section 4.2), respectively.

4.1. Direct lighting using reservoir sampling

Substituting the direct light part of Eq. (6) into Eq. (5) gives the rendering equation of direct light:

$$C_{\text{PBR}}^{\text{dir}}(\mathbf{r}) = \int_{\Omega} V(\mathbf{x}, \omega_i) L_{\text{env}}(\omega_i) f_r(\mathbf{x}, \omega_i, \mathbf{d}, \mathbf{m})(\omega_i \cdot \mathbf{n}) d\omega_i, \quad (9)$$

where $L_{\text{env}}(\omega_i)$ is the environment illumination in direction ω_i , which can be easily obtained by querying the environment map. We estimate this equation using the classic Monte Carlo integration:

$$C_{\text{PBR}}^{\text{dir}}(\mathbf{r}) \approx \frac{1}{N} \sum_{i=1}^N \frac{V(\mathbf{x}, \omega_i) L_{\text{env}}(\omega_i) f_r(\mathbf{x}, \omega_i, \mathbf{d}, \mathbf{m})(\omega_i \cdot \mathbf{n})}{p_{\text{dir}}(\omega_i)} \quad (10)$$

with N samples drawn from some distribution $p_{\text{dir}}(\omega_i)$. In Eq. (10), only $V(\mathbf{x}, \omega_i)$ and $p_{\text{dir}}(\omega_i)$ are unknown, while the remaining terms are either analytically determined or trainable parameters. Therefore, determining $V(\mathbf{x}, \omega_i)$ and finding an appropriate probability distribution $p_{\text{dir}}(\omega_i)$ is key to estimating direct illumination.

Visibility estimation Based on our mesh-based geometry, our method can directly determine $V(\mathbf{x}, \omega_i)$ by ray-mesh intersection in our path tracing framework. With the intersection point \mathbf{x} obtained from `nvdiffrast`, we sample an outgoing direction ω_i to construct the visibility test ray $\mathbf{r}_i(t) = \mathbf{x} + t\omega_i$. Then, we conduct a ray-mesh intersection test to determine whether the ray is occluded. $V(\mathbf{x}, \omega_i)$ will be 0 if $\mathbf{r}_i(t)$ is occluded, otherwise 1. Benefiting from our mesh-based representation, we implement a linear BVH (LBVH [46]) using CUDA kernels to significantly accelerate the ray-mesh intersection calculation. Our LBVH is updated in each iteration to match the mesh refinement. Compared to estimating $V(\mathbf{x}, \omega_i)$ by the transmittance function in volume rendering (which is commonly used by implicit-based methods like TensoIR [22]), our explicit ray-mesh intersection computation is much more efficient, which enables us to increase the sample count for a more precise and low-variance estimation.

Reservoir sampling To reduce the variance of direct lighting estimation (*i.e.* to reduce rendering noise, see Figure 3), we utilize reservoir sampling [25], an advanced resampled importance sampling (RIS) technique [37] to determine the appropriate $p_{\text{dir}}(\omega_i)$. According to the multiple importance sampling (MIS) theory [36], the variance of the Monte Carlo estimator will reduce when $p_{\text{dir}}(\omega_i)$ is closer to the integrand (Eq. (9)). Therefore, when $p_{\text{dir}}(\omega_i)$ is proportional to $L_{\text{env}}(\omega_i) f_r(\mathbf{x}, \omega_i, \mathbf{d}, \mathbf{m})$, the Monte Carlo estimator Eq. (10) will be very efficient. However, it is

impossible to analytically sample from such a probability distribution as it does not have a closed-form expression.

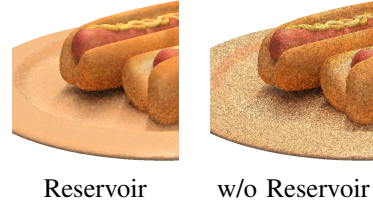


Figure 3. Comparison on rendering noise with or without reservoir sampling with sample count 1. The reservoir sampling can significantly reduce the rendering variance thus speeding up the convergence of inverse rendering.

Instead, we construct a distribution $q_{\text{dir}}(\omega_i)$ that is proportional to $L_{\text{env}}(\omega_i)$ and create m samples $\mathcal{S} = \{\omega_1, \dots, \omega_m\}$ from it. Then we assign a weight $\gamma_i = \frac{p_{\text{dir}}(\omega_i)}{q_{\text{dir}}(\omega_i)}$ to each sample ω_i . Finally, we resample one candidate from \mathcal{S} with a probability proportional to its weight γ_i . This process forms a one-sample RIS estimator of Eq. (9):

$$C_{\text{PBR}}^{\text{dir}}(\mathbf{r}) \approx \frac{1}{N} \sum_{i=1}^N \left(\frac{f(\omega_i)}{p_{\text{dir}}(\omega_i)} \frac{1}{m} \sum_{s=1}^m \frac{p_{\text{dir}}(\omega_s)}{q_{\text{dir}}(\omega_s)} \right), \quad (11)$$

where $f(\omega_i)$ is the integrand in Eq. (9). In addition, we also exploit spatial reuse and temporal reuse, incorporating samples from neighboring pixels and previous frames as candidates in Eq. (11). As illustrated in Figure 3, our reservoir sampling strategy significantly reduces the rendering noise under the same sample count compared to the standard Monte Carlo estimator.

4.2. Indirect lighting using multi-bounce path tracing

Similar to Eqs. (9) and (10), we can also give the rendering equation of indirect light and estimate it by Monte Carlo integration:

$$C_{\text{PBR}}^{\text{ind}}(\mathbf{r}) = \int_{\Omega} L_{\text{ind}}(\mathbf{x}, \omega_i) f_r(\mathbf{x}, \omega_i, \mathbf{d}, \mathbf{m})(\omega_i \cdot \mathbf{n}) d\omega_i, \quad (12)$$

$$\approx \frac{1}{N} \sum_{k=1}^N \frac{L_{\text{ind}}(\mathbf{x}, \omega_i^k) f_r(\mathbf{x}, \omega_i^k, \mathbf{d}, \mathbf{m})(\omega_i^k \cdot \mathbf{n})}{p_{\text{ind}}(\omega_i^k)}. \quad (13)$$

In Eq. (13), after sampling N second-bounce rays $\mathbf{r}_k(t) = \mathbf{x} + t\omega_i^k$ from an appropriate probability distribution $p_{\text{ind}}(\omega_i)$, we need to estimate their radiance values $L_{\text{ind}}(\mathbf{x}, \omega_i)$ to complete the Monte Carlo estimation. The $p_{\text{ind}}(\omega_i)$ of indirect lighting is straightforward: we apply the light importance sampling and GGX importance sampling [39] which is similar to the MIS of NVdiffrec-MC [14], except that we use the power heuristic rather than the balance heuristic. Please refer to PBRT [40] for a detailed description.

Estimating $L_{\text{ind}}(\mathbf{x}, \omega_i)$ is relatively complicated. Most existing inverse rendering methods considering indirect

lighting adopt an implicit strategy to estimate indirect illumination, using neural radiance fields to cache the outgoing radiance values of \mathbf{r}_k . The radiance values of \mathbf{r}_k are estimated by the standard volume rendering process in NeRF. The disadvantage of this strategy is obvious: the accuracy of indirect lighting is determined by the neural radiance field without any physical constraints. NeRF models inevitably contain estimation errors (especially in scenes with high-frequency details), so that the indirect lighting estimation will be biased and inaccurate. In contrast, physically-based rendering methods conduct multi-bounce path tracing to produce an unbiased estimation of $L_{ind}(\mathbf{x}, \omega_i)$. However, due to the low performance of implicit representations, recursively performing multi-bounce path tracing leads to intractable computation. Therefore, the aforementioned implicit strategy can be regarded as a compromise on the computation costs.

Benefiting from our efficient mesh-based representation, we can directly perform path tracing to estimate $L_{ind}(\mathbf{x}, \omega_i)$ as shown in Figure 4. We first sample a new ray $\mathbf{r}_{ind}(t) = \mathbf{x} + t\mathbf{d}_{ind}$ starting from \mathbf{x} as the second bounce, and then we trace $\mathbf{r}_{ind}(t)$ and intersect it with the mesh at point $\hat{\mathbf{x}}$. The indirect lighting is estimated by:

$$\begin{aligned} L_{ind}(\mathbf{x}, \omega_i) &= C_{\text{PBR}}(\mathbf{r}_{ind}) \\ &= \int_{\Omega} L_i(\hat{\mathbf{x}}, \omega_i) f_r(\hat{\mathbf{x}}, \omega_i, \mathbf{d}_{ind}, \hat{\mathbf{m}})(\omega_i \cdot \hat{\mathbf{n}}) d\omega_i. \end{aligned} \quad (14)$$

Note that Eq. (14) is a recursive computation. In practice, we only consider the first three bounces, which balances the computation costs and accuracy. It is also worth mentioning that we detach the gradients of indirect rays due to the limited GPU memory.

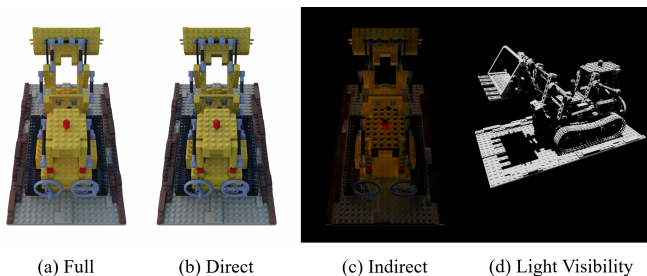


Figure 4. We show our rendering results of direct (b), indirect (c), and full (a) lighting in the *Lego* scene. Note that the sharp light visibility in (d) demonstrates the accuracy of our path-tracing rendering model and our reconstruction geometry.

5. Experiments

In this section, we perform comprehensive experiments to evaluate our method. We compare the performance of our method with state-of-the-art inverse rendering methods and conduct ablation studies to validate the effectiveness of our designs.

Implementation and training details We implement MIRReS using Pytorch framework [42] with CUDA extensions in SLANG.D [47]. We customize CUDA kernels in our rendering layer to perform efficient reservoir sampling and multi-bounce path tracing. We also utilize `nvdiffrast` [12] for differentiable ray-mesh intersection. We run our training and inference on a single NVIDIA RTX 4090 GPU for all our results. The training process of both stages takes about 4.5 hours.

Our training process is described in Section 3, we employ a two-stage training strategy to optimize geometry, material and lighting. The first stage’s training is identical to the standard InstantNGP’s [4] and NeuS2’s [24] training, and we refer to their papers for detailed specifications such as training losses. Our model is trained by rendering loss (Eqs. (7) and (8)) along with several regularization terms. To prevent drastic changes in vertex offset $\Delta\mathbf{v}$ during optimization, we apply the Laplacian smooth loss and vertices offset regularization loss from NeRF2Mesh [11]:

$$\mathcal{L}_{\text{smooth}} = \sum_i \sum_{j \in X_i} \frac{1}{|X_i|} \|(\mathbf{v}_i + \Delta\mathbf{v}_i) - (\mathbf{v}_j + \Delta\mathbf{v}_j)\|^2, \quad (16)$$

$$\mathcal{L}_{\text{offset}} = \sum_i \|\Delta\mathbf{v}_i\|^2, \quad (17)$$

where X_i is the set of adjacent vertex indices of \mathbf{v}_i .

We also apply the smoothness regularizers for albedo \mathbf{k}_d , roughness ρ , and normal \mathbf{n} proposed by NVdiffrec-MC [14] for better intrinsic decomposition:

$$\mathcal{L}_{\mathbf{k}} = \frac{1}{|X|} \sum_{x_i \in X} |\mathbf{k}(\mathbf{x}_i) - \mathbf{k}(\mathbf{x}_i + \epsilon)|, \quad \mathbf{k} \in \{\mathbf{k}_d, \rho, \mathbf{n}\}, \quad (18)$$

where X is the set of world space positions on the surface, and ϵ is a small random offset vector.

Additionally, for better disentangling material parameters and light, we adopt the same monochrome regularization term of NVdiffrec-MC [14]:

$$\mathcal{L}_{\text{light}} = |Y(\mathbf{c}_d + \mathbf{c}_s) - V(I_{\text{ref}})|, \quad (19)$$

where \mathbf{c}_d and \mathbf{c}_s are the demodulated diffuse and specular lighting terms, $Y(\mathbf{x}) = (\mathbf{x}_r + \mathbf{x}_g + \mathbf{x}_b)/3$ is a luminance operator, $V(\mathbf{x}) = \max(\mathbf{x}_r, \mathbf{x}_g, \mathbf{x}_b)$ is the HSV value component. For more details and discussions of this loss, please refer to NVdiffrec-MC [14].

Datasets We perform experiments using 2 benchmark datasets for inverse rendering: the synthetic dataset from TensoIR [22] and the Objects-with-Lighting (OWL) real dataset [45]. The TensoIR dataset contains 4 synthetic scenes with complex illumination effects, with the ground truths of material parameters, geometry, and relighted images. We choose 4 scenes from the OWL dataset, in which each scene contains multi-view real-captured photos of a specific object, and several photos of the same object under a different lighting condition (along with the captured environment map) as the ground truth of relighting evaluation. All objects in the scenes contain spatially-varying materials with complex

Table 2. **QUANTITATIVE COMPARISON OF RECONSTRUCTED MESH, ALBEDO AND RELIGHTING, NOVEL VIEW SYNTHESIS ON TENSORIR DATASET.** METRICS ARE AVERAGED OVER ALL TESTING IMAGES IN SCENES IN THE DATASET. WE HIGHLIGHT THE BEST, SECOND-BEST, THIRD-BEST RESULTS, ACCORDINGLY.

| Method | Geometry | | Albedo | | | Relighting | | | Novel View Synthesis | | |
|---------|-------------------|-------------|--------|-------|--------|------------|-------|--------|----------------------|-------|--------|
| | Chamfer Distance↓ | Normal MAE↓ | PSNR↑ | SSIM↑ | LPIPS↓ | PSNR↑ | SSIM↑ | LPIPS↓ | PSNR↑ | SSIM↑ | LPIPS↓ |
| NVD-MC | 0.073 | 5.050 | 28.875 | 0.957 | 0.082 | 27.810 | 0.907 | 0.110 | 30.036 | 0.949 | 0.083 |
| TensoIR | 0.083 | 4.100 | 29.275 | 0.950 | 0.085 | 28.580 | 0.944 | 0.081 | 35.088 | 0.976 | 0.040 |
| GS-IR | N/A | 4.948 | 30.286 | 0.941 | 0.084 | 24.374 | 0.885 | 0.096 | 35.333 | 0.974 | 0.039 |
| Ours | 0.056 | 3.305 | 32.348 | 0.970 | 0.054 | 32.363 | 0.965 | 0.055 | 35.260 | 0.976 | 0.042 |

global illumination effects, including diffuse inter-reflections and specular highlights, making the inverse rendering task highly challenging. We’ll show the results of our method later.

Metrics To assess the quality of the reconstructed geometry, we use the mean angular error (MAE) of the reconstructed normal and the chamfer distance of the reconstructed mesh. As for intrinsic decomposition, we evaluate the quality of reconstructed albedo, novel view synthesis of physically-based surface rendering, and the relighting results. We use the widely-used Peak Signal-to-Noise Ratio (PSNR), Structural Similarity Index Measure (SSIM), and Learned Perceptual Image Patch Similarity (LPIPS) as the evaluation metrics. It is worth mentioning that due to the inherent ambiguity between the scale of albedo and illumination, we adopt a similar scaling strategy to TensoIR [22]. For the TensoIR dataset, each RGB channel of all albedo results is scaled by a global scalar; for the OWL dataset, the exposure level for each relighting result is also scaled.

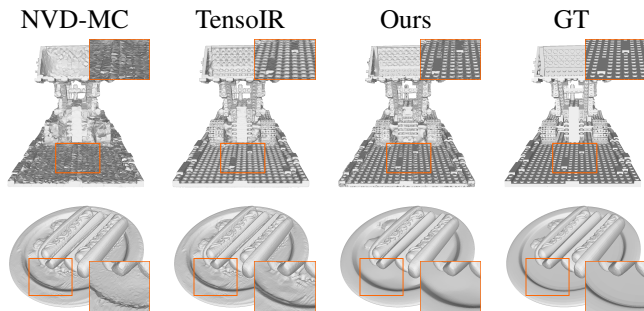


Figure 5. **Qualitative comparison of the reconstructed mesh on TensoIR dataset.**

5.1. Comparisons

We compare qualitative and quantitative results with state-of-the-art methods, including TensoIR [22], GS-IR [16], NVdiffrec-MC [14] (labeled as NVD-MC in the following figures and tables), as the representatives of implicit-based, 3DGS-based and mesh-based inverse rendering frameworks. We’ll demonstrate that our method outperforms all these works owing to our novel design.

Comparison on geometry reconstruction The first two columns in Table 2 report the quantitative comparisons of

the normal MAE and the chamfer distance between the reconstructed mesh and the ground truth mesh. On average, our method achieves the best results, with a 23.3% lower error on mesh and a 19.4% lower error on normal compared to the second-best baseline. We also provide qualitative results of the reconstructed mesh in Figure 5 and the normal map in the last row in Figure 6. Note that GS-IR does not support mesh extraction, so the chamfer distance is not applicable. TensoIR’s geometry is incapable of recovering high-frequency details and sharp edges because of the inherent low expressive capacity of implicit density fields, while NVdiffrec-MC suffers from artifacts such as holes and uneven surfaces. Their geometry quality also suffers from specular surfaces, such as the dish in the *Hotdog* scene. Thanks to our two-stage strategy, our refined meshes and normals demonstrate superior quality.

Comparison on decomposition and relighting results We perform a comprehensive comparison of the decomposed albedo, environment lighting and novel view synthesis results by PBR rendering. In this paragraph, we’ll report both qualitative and quantitative results on TensoIR dataset and OWL dataset, respectively.

TensoIR dataset Qualitatively, as shown in Figure 6, our method produces superior decomposition results to all baselines. TensoIR and GS-IR have difficulties in correctly decomposing the lighting effects from the materials, leading to artifacts such as baked-in shadows on the albedo texture. NVdiffrec-MC produces suboptimal results due to their unstable geometry reconstruction, resulting in hole-like artifacts. On the other hand, thanks to our physically-based design to capture direct and indirect lighting, we successfully produce high-quality recovered material, eliminating the highly challenging shadow-like artifacts on the material textures. In addition, we also select several environment maps to evaluate relighting results, and illustrate per-scene decomposition and relighting results in Figure 11 and Figure 12. Owing to our more accurate material estimation, we produce more realistic relighting results, including more accurate shadows, specular highlights and inter-reflections.

Further, we also report quantitative comparisons in Table 2, where our method achieves significant advantages over baselines in albedo and relighting results. Note that in terms of novel view synthesis, our method demonstrates similar performance compared to TensoIR and GS-IR. This is because these baselines tend to overfit the training dataset and bake the complex lighting effects (*e.g.* shadows) within

the materials, as qualitatively analyzed above. Despite this, we can produce considerably better material estimation and relighting results.

Objects-with-Lighting (OWL) dataset We provide per-scene qualitative comparisons on the real-captured OWL dataset in Figure 13 and Figure 14. We incorporate metallic learning as an additional channel in the materials network for this dataset. Our method demonstrates superior quality in the relighting appearances, while baseline methods suffer from color bias (e.g. *Tpiece* scene in Figure 13), incorrect lighting effects (e.g. highlights in *Gamepad* scene in Figure 14) or missing details (e.g. textures in *Antman* scene in Figure 13). Although it is impossible to obtain ground truth material parameters in the real dataset, it can be intuitively observed that our method produces more reasonable material estimations. We also report quantitative comparisons on relighting and novel view synthesis in Table 3, where our method achieves the best scores in all metrics.

Table 3. QUANTITATIVE COMPARISON OF NOVEL VIEW SYNTHESIS AND RELIGHTING ON OBJECT-WITH-LIGHTING DATASET. METRICS ARE AVERAGED OVER ALL TESTING IMAGES IN SCENES: ANTMAN, TPIECE, GAMEPAD, PORCELAIN MUG OF THE DATASET.

| Method | Relighting | | | Novel View Synthesis | | |
|---------|-----------------|-----------------|--------------------|----------------------|-----------------|--------------------|
| | PSNR \uparrow | SSIM \uparrow | LPIPS \downarrow | PSNR \uparrow | SSIM \uparrow | LPIPS \downarrow |
| NVD-MC | 21.110 | 0.970 | 0.066 | 34.409 | 0.967 | 0.059 |
| TensoIR | 26.382 | 0.966 | 0.038 | 37.127 | 0.985 | 0.045 |
| GS-IR | 18.761 | 0.101 | 0.314 | 30.527 | 0.793 | 0.096 |
| Ours | 28.827 | 0.977 | 0.031 | 38.223 | 0.986 | 0.030 |

5.2. Ablation Studies

Reservoir sampling and multi-bounce raytracing We conduct ablation studies to verify the effectiveness of our two key designs — reservoir sampling and multi-bounce raytracing. We quantitatively compare the albedo PSNR in Table 4 using models with or without reservoir sampling and multi-bounce raytracing. The results show that both design

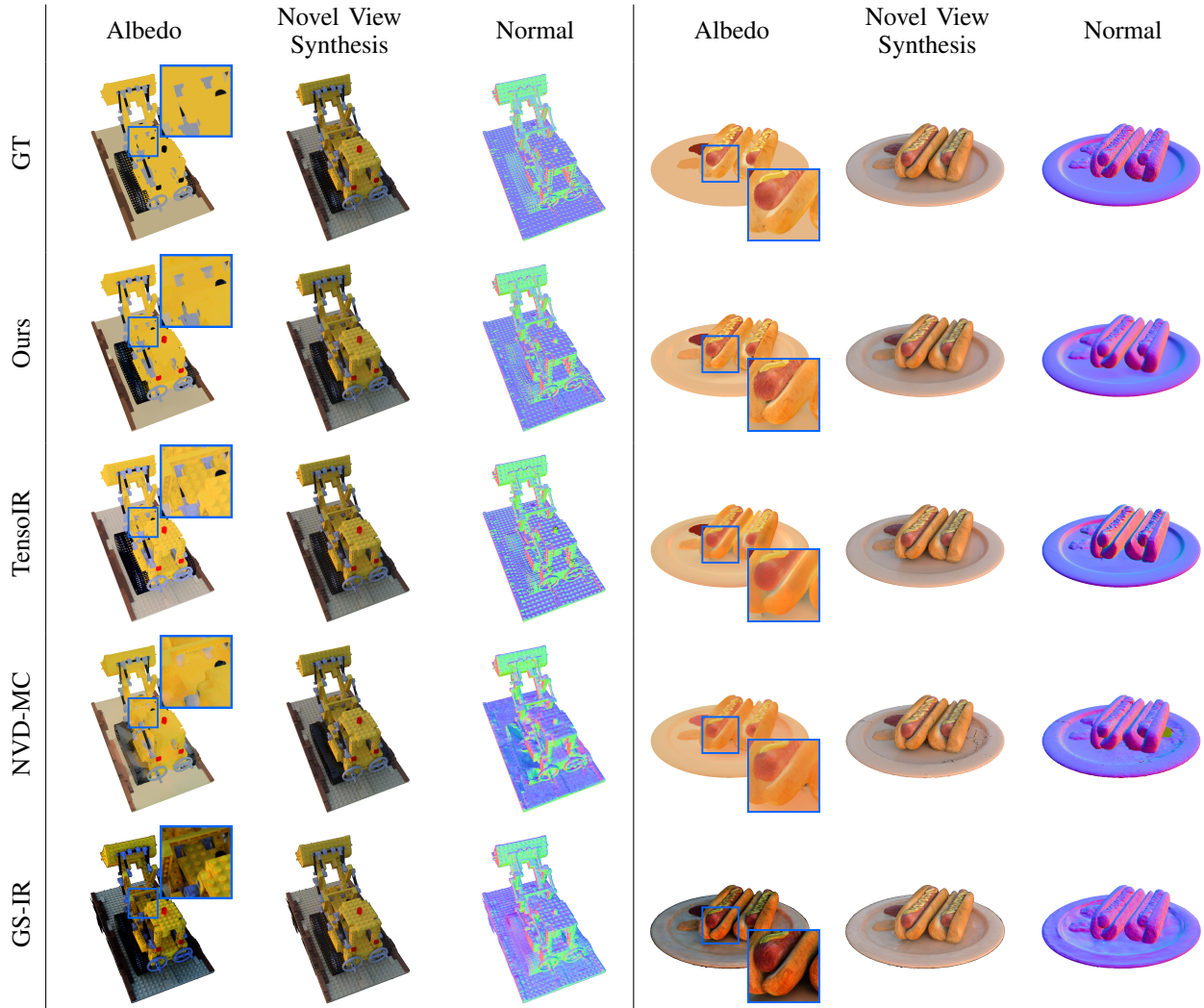


Figure 6. Qualitative comparison of albedo and PBR rendering results on TensoIR dataset. Zoom in for details.

contributes to the increase of PSNR and the full model demonstrates optimal performance.

Table 4. ABLATION STUDIES ON RESERVOIR SAMPLING AND MULTI-BOUNCE RAYTRACING.

| Reservoir | Multi-bounce | Albedo PSNR | Relighting PSNR |
|-----------|--------------|-------------|-----------------|
| ✗ | ✗ | 31.950 | 28.992 |
| ✓ | ✗ | 32.529 | 31.239 |
| ✗ | ✓ | 33.752 | 31.694 |
| ✓ | ✓ | 34.348 | 33.788 |



Figure 7. **Ablation studies on indirect illumination.** The specular reflection around the plate is heavily embedded into the reconstruction albedo because of the absence of indirect illumination, whereas our method recovers a cleaner albedo.

Indirect illumination Figure 7 illustrates the reconstructed albedo using our full model and an ablation model without indirect lighting, verifying that introducing indirect illumination can significantly improve the quality of material estimation.

Number of SPPs We evaluate the novel view synthesis PSNR of the *hotdog* scene with 4 different configurations under different SPPs (from 4 to 64) in Figure 8. The 4 configurations consist of path tracing without indirect illumination (PT), path tracing with indirect illumination (PT full), path tracing with reservoir sampling but without indirect illumination (ReSTIR), and path tracing with both reservoir sampling and indirect illumination (ReSTIR full). Figure 8 shows that the “ReSTIR full” configuration, *i.e.* the full configuration of our method, achieves the highest PSNR among all SPPs which verifies the effectiveness of reservoir sampling and indirect illumination. Note that although the PSNR of “PT” is higher than “PT full”, this does not mean the indirect illumination has a negative effect. Due to the lack of indirect illumination, “PT” bakes the specular reflection into the albedo, while “PT full” cannot capture the specular reflections due to the severe rendering noise at low SPP. As SPP increases, the specular reflections reconstructed by “PT full” become more accurate, while lower rendering variance leads to more specular ambiguity in “PT”, causing a decline in PSNR. At the same time, Figure 8 shows that a configuration with SPP higher than 32 does not necessarily improve the reconstruction accuracy. Thus, we use 32 SPP as the default configuration for all our experiments in this section.

Neural radiance field rendering As described in Section 3.2, we employ two rendering methods: neural radiance field rendering and physically-based surface rendering to jointly optimize the reconstructed geometry. Here we demonstrate the necessity of the neural radiance field rendering. As can be seen from Figure 9, surface-only rendering (the third column) leads to incorrect geometry, which in turn affects the materials’ reconstruction.

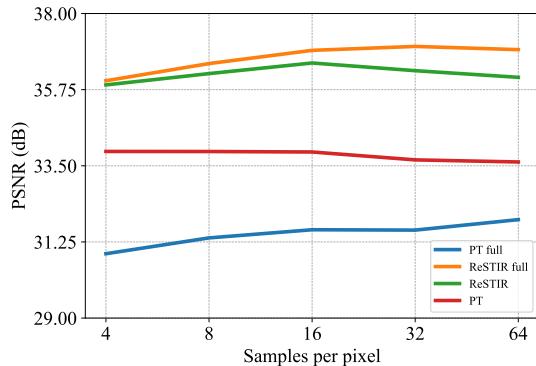


Figure 8. Novel view synthesis PSNR of *hotdog* with different SPPs.

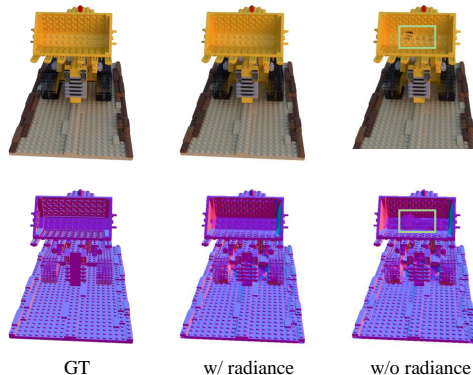


Figure 9. **Effect of neural radiance field rendering.** The first row is the novel view synthesis results, and the second row is the reconstructed normal.

6. Conclusion

In this work, we present a two-stage physically-based inverse rendering framework that jointly reconstructs and optimizes the explicit geometry, material, and illumination from multi-view images. In stage 1, we train a neural radiance field and extract a coarse mesh as our initial geometry. In stage 2, we refine the mesh geometry by trainable offsets, and optimize material and illumination by a physically-based inverse rendering model that utilizes multi-bounce path tracing and Monte Carlo integration. To speed up the convergence of Monte Carlo rendering, we introduce the reservoir sampling algorithm along with multi-importance sampling to reduce variance and maintain low rendering noise at a low sample count. Experiments on challenging scenarios with complex shadows demonstrate that our method achieves state-of-the-art performance on the decomposition results.

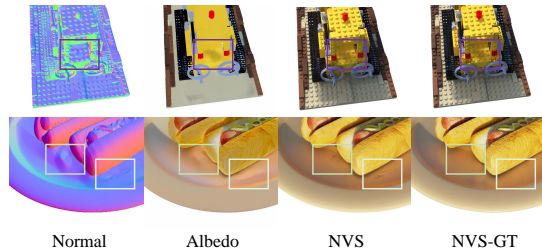


Figure 10. **Limitation: incorrect material estimation on the NeRF synthetic dataset.** The first row is the *lego* results, the second row is the *hotdog* results.

Limitation and future work The performance of our optimization relies on the initial coarse geometry from stage 1. Although NeuS2 can reconstruct plausible geometry in most cases, the extracted mesh still contains obvious errors in particular areas, *e.g.* highly specular regions or high-frequency details, resulting in incorrect material estimation and novel view synthesis at the corresponding area (see Figure 10). How to improve the geometry optimization capabilities is left as a future work. Furthermore, our physically-based inverse rendering framework does not consider the gradients of non-primary rays. These gradients may increase the reconstruction accuracy, while they’ll take up a lot of GPU memory and significantly increase the computational overhead. We leave the investigation of efficient and compact gradient computation as our future work.

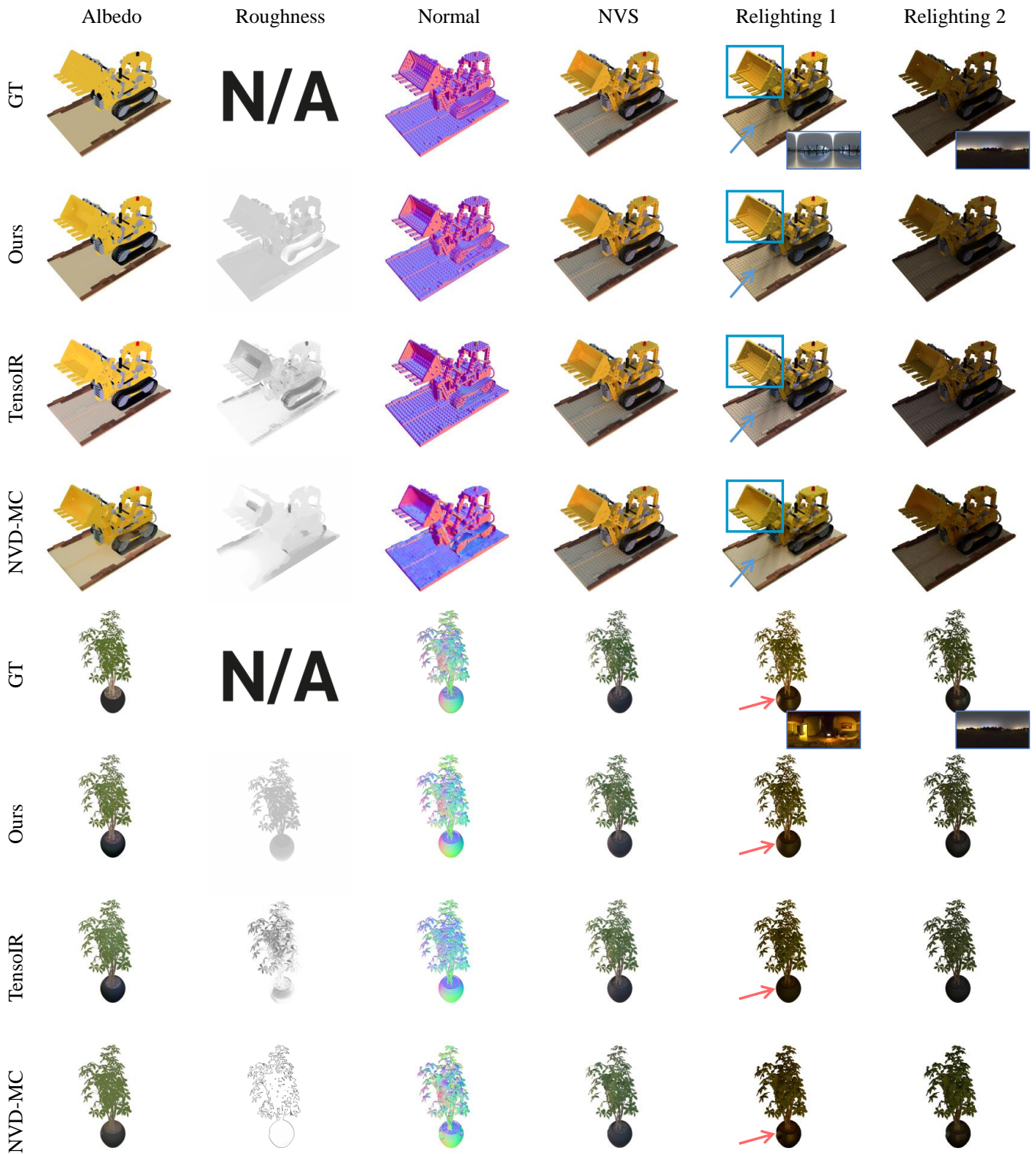


Figure 11. Qualitative results on *Lego* and *Ficus* scenes in TensorIR dataset. The corresponding environment map for relighting is placed on the bottom right of the GT relighting result.

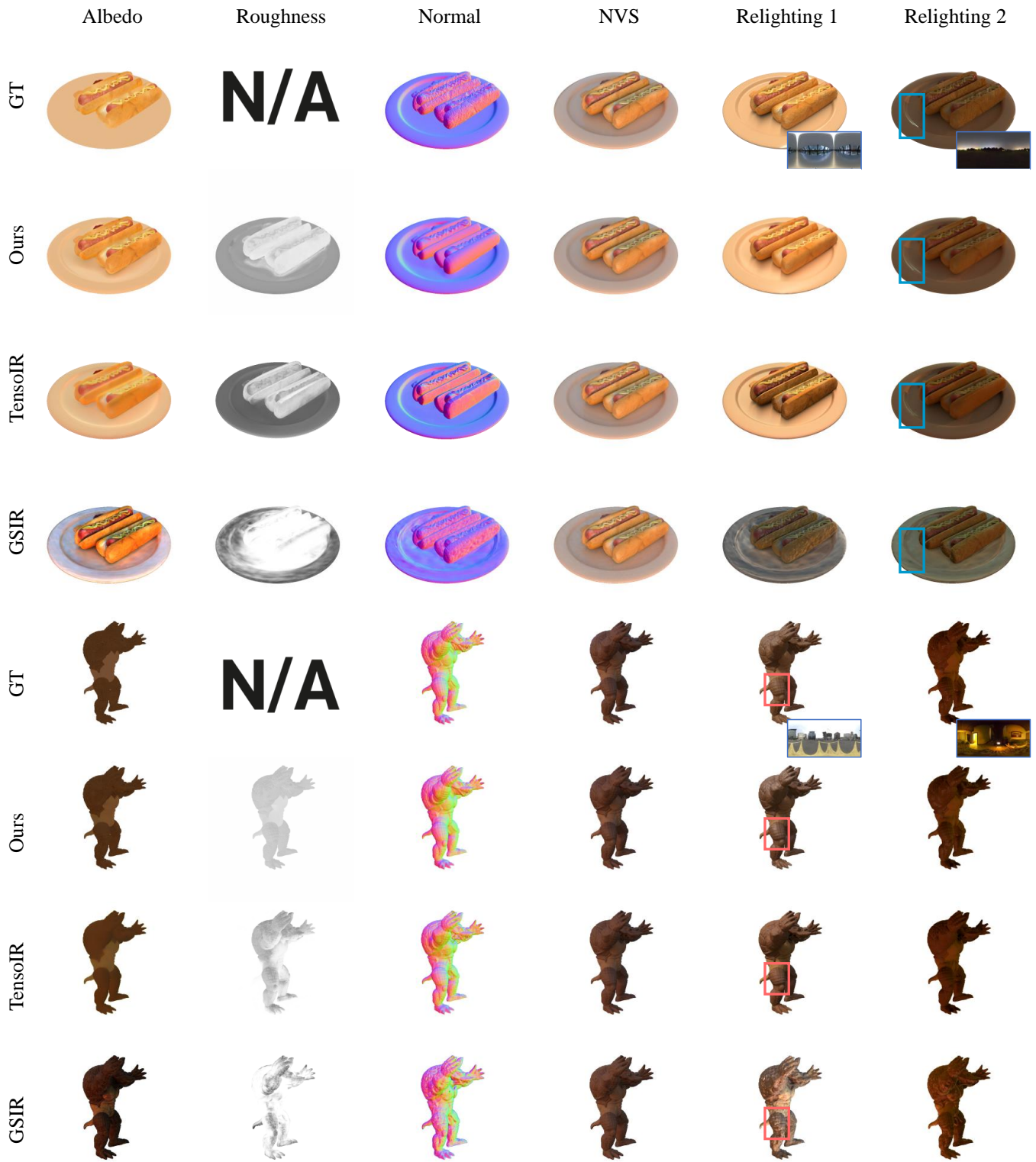


Figure 12. Qualitative results on *Hotdog* and *Armadillo* scenes in *TensorIR* dataset. The corresponding environment map for relighting is placed on the bottom right of the GT relighting result.

















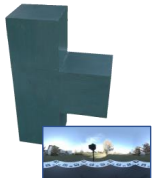















| | Albedo | Roughness | Metallic | Relighting 1 | Relighting 2 |
|----------|---|---|---|--|---|
| GT | N/A | N/A | N/A |  |  |
| Ours |  |  |  |  |  |
| TensorIR |  |  | N/A |  |  |
| NVD-MC |  |  |  |  |  |
| GT | N/A | N/A | N/A |  |  |
| Ours |  |  |  |  |  |
| TensorIR |  |  | N/A |  |  |
| NVD-MC |  |  |  |  |  |

Figure 13. Qualitative comparison on Object-with-Lighting dataset (part 1). Chosen from *Antman* and *Tpiece* scenes.



Figure 14. Qualitative comparison on Object-with-Lighting dataset (part 2). Chosen from *Gamepad* and *Mug* scenes.

References

- [1] B. Mildenhall, P. P. Srinivasan, M. Tancik, J. T. Barron, R. Ramamoorthi, and R. Ng, "Nerf: Representing scenes as neural radiance fields for view synthesis," *Communications of the ACM*, vol. 65, no. 1, pp. 99–106, 2021.
- [2] S. Fridovich-Keil, A. Yu, M. Tancik, Q. Chen, B. Recht, and A. Kanazawa, "Plenoxels: Radiance fields without neural networks," in *Proceedings of the IEEE/CVF Conference on Computer Vision and Pattern Recognition*, 2022, pp. 5501–5510.
- [3] C. Sun, M. Sun, and H.-T. Chen, "Direct voxel grid optimization: Super-fast convergence for radiance fields reconstruction," in *Proceedings of the IEEE/CVF Conference on Computer Vision and Pattern Recognition*, 2022, pp. 5459–5469.
- [4] T. Müller, A. Evans, C. Schied, and A. Keller, "Instant neural graphics primitives with a multiresolution hash encoding," *ACM transactions on graphics (TOG)*, vol. 41, no. 4, pp. 1–15, 2022.
- [5] A. Chen, Z. Xu, A. Geiger, J. Yu, and H. Su, "Tensorf: Tensorial radiance fields," in *European Conference on Computer Vision*. Springer, 2022, pp. 333–350.
- [6] Z. Chen, T. Funkhouser, P. Hedman, and A. Tagliasacchi, "Mobilenerf: Exploiting the polygon rasterization pipeline for efficient neural field rendering on mobile architectures," in *Proceedings of the IEEE/CVF Conference on Computer Vision and Pattern Recognition*, 2023, pp. 16569–16578.
- [7] Z. Wang, T. Shen, M. Nimier-David, N. Sharp, J. Gao, A. Keller, S. Fidler, T. Müller, and Z. Gojic, "Adaptive shells for efficient neural radiance field rendering," *ACM Transactions on Graphics (TOG)*, vol. 42, no. 6, pp. 1–15, 2023.
- [8] P. Wang, L. Liu, Y. Liu, C. Theobalt, T. Komura, and W. Wang, "Neus: Learning neural implicit surfaces by volume rendering for multi-view reconstruction," *Advances in Neural Information Processing Systems*, vol. 34, pp. 27 171–27 183, 2021.
- [9] L. Yariv, J. Gu, Y. Kasten, and Y. Lipman, "Volume rendering of neural implicit surfaces," *Advances in Neural Information Processing Systems*, vol. 34, pp. 4805–4815, 2021.
- [10] B. Kerbl, G. Kopanas, T. Leimkühler, and G. Drettakis, "3d gaussian splatting for real-time radiance field rendering," *ACM Transactions on Graphics*, vol. 42, no. 4, pp. 1–14, 2023.
- [11] J. Tang, H. Zhou, X. Chen, T. Hu, E. Ding, J. Wang, and G. Zeng, "Delicate textured mesh recovery from nerf via adaptive surface refinement," in *Proceedings of the IEEE/CVF International Conference on Computer Vision*, 2023, pp. 17 739–17 749.
- [12] S. Laine, J. Hellsten, T. Karras, Y. Seol, J. Lehtinen, and T. Aila, "Modular primitives for high-performance differentiable rendering," *ACM Transactions on Graphics*, vol. 39, no. 6, 2020.
- [13] B. Burley and W. D. A. Studios, "Physically-based shading at disney," in *Acm Siggraph*, vol. 2012. vol. 2012, 2012, pp. 1–7.
- [14] J. Hasselgren, N. Hofmann, and J. Munkberg, "Shape, light, and material decomposition from images using monte carlo rendering and denoising," *Advances in Neural Information Processing Systems*, vol. 35, pp. 22 856–22 869, 2022.
- [15] X. Zhang, P. P. Srinivasan, B. Deng, P. Debevec, W. T. Freeman, and J. T. Barron, "Nerfactor: Neural factorization of shape and reflectance under an unknown illumination," *ACM Transactions on Graphics (ToG)*, vol. 40, no. 6, pp. 1–18, 2021.
- [16] Z. Liang, Q. Zhang, Y. Feng, Y. Shan, and K. Jia, "Gs-ir: 3d gaussian splatting for inverse rendering," *arXiv preprint arXiv:2311.16473*, 2023.
- [17] P. P. Srinivasan, B. Deng, X. Zhang, M. Tancik, B. Mildenhall, and J. T. Barron, "Nerv: Neural reflectance and visibility fields for relighting and view synthesis," in *Proceedings of the IEEE/CVF Conference on Computer Vision and Pattern Recognition*, 2021, pp. 7495–7504.
- [18] M. Boss, R. Braun, V. Jampani, J. T. Barron, C. Liu, and H. Lensch, "Nerf: Neural reflectance decomposition from image collections," in *Proceedings of the IEEE/CVF International Conference on Computer Vision*, 2021, pp. 12 684–12 694.
- [19] M. Boss, V. Jampani, R. Braun, C. Liu, J. Barron, and H. Lensch, "Neural-pil: Neural pre-integrated lighting for reflectance decomposition," *Advances in Neural Information Processing Systems*, vol. 34, pp. 10 691–10 704, 2021.
- [20] Y. Zhang, J. Sun, X. He, H. Fu, R. Jia, and X. Zhou, "Modeling indirect illumination for inverse rendering," in *Proceedings of the IEEE/CVF Conference on Computer Vision and Pattern Recognition*, 2022, pp. 18 643–18 652.
- [21] K. Zhang, F. Luan, Q. Wang, K. Bala, and N. Snavely, "Physg: Inverse rendering with spherical gaussians for physics-based material editing and relighting," in *Proceedings of the IEEE/CVF Conference on Computer Vision and Pattern Recognition*, 2021, pp. 5453–5462.
- [22] H. Jin, I. Liu, P. Xu, X. Zhang, S. Han, S. Bi, X. Zhou, Z. Xu, and H. Su, "Tensoir: Tensorial inverse rendering," in *Proceedings of the IEEE/CVF Conference on Computer Vision and Pattern Recognition*, 2023, pp. 165–174.
- [23] H. Wu, Z. Hu, L. Li, Y. Zhang, C. Fan, and X. Yu, "Nefii: Inverse rendering for reflectance decomposition with near-field indirect illumination," in *Proceedings of the IEEE/CVF Conference on Computer Vision and Pattern Recognition*, 2023, pp. 4295–4304.
- [24] Y. Wang, Q. Han, M. Habermann, K. Daniilidis, C. Theobalt, and L. Liu, "Neus2: Fast learning of neural implicit surfaces for multi-view reconstruction," in *Proceedings of the IEEE/CVF International Conference on Computer Vision*, 2023, pp. 3295–3306.
- [25] B. Bitterli, C. Wyman, M. Pharr, P. Shirley, A. Lefohn, and W. Jarosz, "Spatiotemporal reservoir resampling for real-time ray tracing with dynamic direct lighting," *ACM Transactions on Graphics (TOG)*, vol. 39, no. 4, pp. 148–1, 2020.
- [26] S. Bi, Z. Xu, K. Sunkavalli, M. Hašan, Y. Hold-Geoffroy, D. Kriegsmann, and R. Ramamoorthi, "Deep reflectance volumes: Relightable reconstructions from multi-view photometric images," in *Computer Vision—ECCV 2020: 16th European Conference, Glasgow, UK, August 23–28, 2020, Proceedings, Part III 16*. Springer, 2020, pp. 294–311.
- [27] F. Luan, S. Zhao, K. Bala, and Z. Dong, "Unified shape and svbrdf recovery using differentiable monte carlo rendering," in *Computer Graphics Forum*, vol. 40, no. 4. Wiley Online Library, 2021, pp. 101–113.
- [28] G. Nam, J. H. Lee, D. Gutierrez, and M. H. Kim, "Practical svbrdf acquisition of 3d objects with unstructured flash photography," *ACM Transactions on Graphics (TOG)*, vol. 37, no. 6, pp. 1–12, 2018.
- [29] J. Munkberg, J. Hasselgren, T. Shen, J. Gao, W. Chen, A. Evans, T. Müller, and S. Fidler, "Extracting triangular 3d models, materials, and lighting from images," in *Proceedings of the IEEE/CVF Conference on Computer Vision and Pattern Recognition*, 2022, pp. 8280–8290.
- [30] J. Zhang, Y. Yao, S. Li, J. Liu, T. Fang, D. McKinnon, Y. Tsin, and L. Quan, "Neif++: Inter-reflectable light fields for geometry and material estimation," in *Proceedings of the IEEE/CVF International Conference on Computer Vision*, 2023, pp. 3601–3610.
- [31] C. Zhang, B. Miller, K. Yan, I. Gkioulekas, and S. Zhao, "Path-space differentiable rendering," *ACM Transactions on Graphics (TOG)*, vol. 39, no. 4, pp. 143–1, 2020.
- [32] T.-M. Li, M. Aittala, F. Durand, and J. Lehtinen, "Differentiable monte carlo ray tracing through edge sampling," *ACM Transactions on Graphics (TOG)*, vol. 37, no. 6, pp. 1–11, 2018.
- [33] J. T. Kajiya, "The rendering equation," in *Proceedings of the 13th annual conference on Computer graphics and interactive techniques*, 1986, pp. 143–150.

- [34] G. Loubet, N. Holzschuch, and W. Jakob, "Reparameterizing discontinuous integrands for differentiable rendering," *ACM Transactions on Graphics (TOG)*, vol. 38, no. 6, pp. 1–14, 2019.
- [35] W. Jakob, S. Speierer, N. Roussel, and D. Vicini, "Dr. jit: A just-in-time compiler for differentiable rendering," *ACM Transactions on Graphics (TOG)*, vol. 41, no. 4, pp. 1–19, 2022.
- [36] E. Veach and L. J. Guibas, "Optimally combining sampling techniques for monte carlo rendering," in *Proceedings of the 22nd annual conference on Computer graphics and interactive techniques*, 1995, pp. 419–428.
- [37] J. F. Talbot, *Importance resampling for global illumination*. Brigham Young University, 2005.
- [38] D. Verbin, P. Hedman, B. Mildenhall, T. Zickler, J. T. Barron, and P. P. Srinivasan, "Ref-nerf: Structured view-dependent appearance for neural radiance fields," in *2022 IEEE/CVF Conference on Computer Vision and Pattern Recognition (CVPR)*. IEEE, 2022, pp. 5481–5490.
- [39] E. Heitz, "Sampling the ggx distribution of visible normals," *Journal of Computer Graphics Techniques (JCGT)*, vol. 7, no. 4, pp. 1–13, 2018.
- [40] M. Pharr, W. Jakob, and G. Humphreys, *Physically based rendering: From theory to implementation*. MIT Press, 2023.
- [41] T. Shen, J. Gao, K. Yin, M.-Y. Liu, and S. Fidler, "Deep marching tetrahedra: a hybrid representation for high-resolution 3d shape synthesis," *Advances in Neural Information Processing Systems*, vol. 34, pp. 6087–6101, 2021.
- [42] A. Paszke, S. Gross, F. Massa, A. Lerer, J. Bradbury, G. Chanan, T. Killeen, Z. Lin, N. Gimeshain, L. Antiga *et al.*, "Pytorch: An imperative style, high-performance deep learning library," *Advances in neural information processing systems*, vol. 32, 2019.
- [43] Z. Yu, A. Chen, B. Huang, T. Sattler, and A. Geiger, "Mip-splatting: Alias-free 3d gaussian splatting," 2024.
- [44] J. Tang, J. Ren, H. Zhou, Z. Liu, and G. Zeng, "Dreamgaussian: Generative gaussian splatting for efficient 3d content creation," in *The Twelfth International Conference on Learning Representations*, 2023.
- [45] B. Ummerhofer, S. Agrawal, R. Sepúlveda, Y. Lao, K. Zhang, T. Cheng, S. R. Richter, S. Wang, and G. Ros, "Objects with lighting: A real-world dataset for evaluating reconstruction and rendering for object relighting," in *3DV*. IEEE, 2024.
- [46] T. Karras, "Maximizing parallelism in the construction of bvhs, octrees, and k-d trees," in *Proceedings of the Fourth ACM SIGGRAPH/Eurographics Conference on High-Performance Graphics*, 2012, pp. 33–37.
- [47] S. Bangaru, L. Wu, T.-M. Li, J. Munkberg, G. Bernstein, J. Ragan-Kelley, F. Durand, A. Lefohn, and Y. He, "Slang.d: Fast, modular and differentiable shader programming," *ACM Transactions on Graphics (SIGGRAPH Asia)*, vol. 42, no. 6, pp. 1–28, December 2023.